PNAS RESEARCH ARTICLE | CHEMISTRY
BIOPHYSICS AND COMPUTATIONAL BIOLOGY

Quantitative insights into the mechanism of proton conduction and selectivity for the human voltage-gated proton channel Hv1

Yu Liu[a], Chenghan Li[a], J. Alfredo Freites[b], Douglas J. Tobias[b], and Gregory A. Voth[a,1]

Edited by Victor Batista, Yale University, New Haven, Connecticut; received April 14, 2024; accepted August 9, 2024 by Editorial Board Member J. A. McCammon

Human voltage-gated proton (hHv1) channels are crucial for regulating essential biological processes such as immune cell respiratory burst, sperm capacitation, and cancer cell migration. Despite the significant concentration difference between protons and other ions in physiological conditions, hHv1 demonstrates remarkable proton selectivity. Our calculations of single-proton, cation, and anion permeation free energy profiles quantitatively demonstrate that the proton selectivity of the wild-type channel originates from its strong proton affinity via the titration of the key residues D112 and D174, although the channel imposes similar kinetic blocking effects for protons compared to other ions. A two-proton knock-on model is proposed to mathematically explain the electrophysiological measurements of the pH-dependent proton conductance in the conductive state. Moreover, it is shown that the anion selectivity of the D112N mutant channel is tied to impaired proton transport and substantial anion leakage.

proton channel | ion selectivity | proton transport | molecular dynamics

Significance

The almost perfect proton selectivity of the human voltage-gated proton (hHv1) channels is a long-standing mystery. The extensive multiscale simulations in this paper offer quantitative insight into the mechanism behind the selective proton transport in hHv1 channels and the altered selectivity toward anions in its D112N mutant. These findings reveal the crucial role of pore-lining residue titrations in the proton permeation and selectivity while ruling out a purely water-mediated proton conduction mechanism.

Human voltage-gated proton channels (hHv1) are widely acknowledged for their immense clinical significance, as they play pivotal roles in a diverse array of fundamental biological processes (1–3). These processes encompass the intricate regulation of respiratory bursts in immune cells (4–6), which are essential for effective immune response against pathogens and tissue damage. Additionally, hHv1 channels contribute to the sperm capacitation process (6, 7), facilitating the acquisition of fertilization competence by spermatozoa. The hHv1 channels are also involved in cancer cell migration (8–10), a crucial step in tumor progression and metastasis. The multifaceted involvement of hHv1 channels in such critical biological processes highlights their significance and underscores the need for a comprehensive understanding of their functional properties and underlying mechanisms.

The essential role of hHv1 in the processes mentioned above is to rapidly extrude protons to regulate pH and to minimize changes in membrane potential due to other electrogenic transporters. One of the most fascinating properties of this ion channel is its remarkable proton selectivity (11) when compared to other cations under a depolarized membrane potential. The proton selectivity has been demonstrated by experimental measurement of the reversal potential (V_{rev}, the membrane potential at zero current), which aligns with the Nernst potential of protons. Considering that protons are a million times less concentrated than other ions under physiological conditions, the remarkable proton selectivity observed necessitates a permeability ratio between protons over other ions ranging from 10^6 to 10^8 (12). To further understand the underlying mechanism of such proton selectivity, numerous experimental and computational attempts have been made to identify key residues and potential proton conduction pathways.

Musset et al. (13) identified D112 as a crucial residue for proton selectivity via electrophysiological measurements. The D112N mutation was found to shift the channel toward anion selectivity, while the D112E mutant maintains proton selectivity. These findings highlight the potential role of titratability and electrostatic effects of D112 in the channel proton selectivity. A follow-up quantum mechanical study (14) on a gas-phase model suggested that the D112-R211 salt bridge acts as a gatekeeper, blocking the passage of other cations while allowing protons to permeate by undergoing protonation and deprotonation at D112. Additionally, both hybrid quantum mechanics/molecular mechanics (QM/MM) (15) and empirical valence bond (16) (EVB) molecular dynamics (MD) simulations provided evidence that explicit proton passage occurs via the titration of D112. However, the high computational cost of QM/MM prevented a converged free energy profile for the proton permeation to be obtained, and thus, a clear conclusion on the proton permeation mechanism could not be obtained. The EVB model by Lee et al. (16) did not fully include the Grotthuss proton hopping transport inside the channel and instead only modeled a shared proton between D112 and its first solvation shell water.

Author affiliations: [a]Department of Chemistry, Chicago Center for Theoretical Chemistry, Institute for Biophysical Dynamics, and James Frank Institute, University of Chicago, Chicago, IL 60637; and [b]Department of Chemistry, University of California, Irvine, CA 92697

Author contributions: J.A.F. and D.J.T. provided the conductive WT Hv1 channel structure; Y.L., C.L., J.A.F., D.J.T., and G.A.V. designed the simulations; Y.L. performed the simulations; Y.L. performed calculations; Y.L. and C.L. derived the equations; Y.L., C.L., J.A.F., D.J.T., and G.A.V. analyzed the result; D.J.T. and G.A.V. supervised the work; and Y.L., C.L., J.A.F., D.J.T., and G.A.V. wrote the paper.

The authors declare no competing interest.

This article is a PNAS Direct Submission. V.S.B. is a Guest Editor invited by the Editorial Board.

[1]To whom correspondence may be addressed. Email: gavoth@uchicago.edu.

This article contains supporting information online at https://www.pnas.org/lookup/suppl/doi:10.1073/pnas.2407479121/-/DCSupplemental.

Published September 11, 2024.

The D112 titration hypothesis implies that the selectivity filter (SF) consists of D112 and its close-by residues, R211 and D185, while imposing greater restrictions on ions other than protons. Thus, this particular hypothesis resembles a more conventional selectivity mechanism in other ion channels.

On the other hand, an alternative "water-wire" viewpoint argues that the SF region provides sufficient space and hydration, allowing excess protons to pass through. Ramsey et al. found (17) that neutralizing each of the conserved titratable residues (D174A, E153A, K157A, D185A, D112A, and D112N) was insufficient to abolish the conductance, and thus, they concluded that the only possible proton permeation mechanism should be Grotthuss transport via a robust continuous water wire. Evidence from classical MD simulations (17–20) has in fact revealed the presence of a persistent water wire within the selective filter region, suggesting an involvement in the proton conduction pathway. In contrast to these four studies, other MD simulations of open-state models have identified "dry" regions within the pore. These studies reported statistically rare (21) and highly transient water wires, lasting only around 6 picoseconds (22), which is too brief to facilitate effective proton transport. Due to the limited and ambiguous structural information available, especially for the open state, the outcome of MD simulations depends on the chosen model, which can vary. Furthermore, explicit proton transport with a dynamic hydration environment is generally required in order to fully understand proton transport in confined spaces since a continuous water wire observed in standard MD without an explicit proton can exhibit distinctive properties from one (the physically correct one) having the presence of an explicit excess proton (23–27).

The determination of the proton permeation and selectivity mechanism of hHv1 has been hindered by the significant challenge to resolve a conductive structure due to the pronounced conformational changes in response to membrane potential and pH gradients (28–30). However, advances in computers (31) have now opened new avenues for studying the physiologically relevant conductive structure of these channels (32). Previously, this challenge was addressed by performing atomistic MD simulations of hHv1 in an explicit membrane environment and under an applied membrane potential on the 10-μs timescale to generate structural models consistent with both the closed and open states of the channel according to the available experimental evidence (32). Subsequent progress has been made in hHv1 inhibitor discovery from classical MD simulations based on this open-state structural model (33–35). However, there is still a clear need for explicit proton permeation simulations to uncover the precise molecular determinants that govern the selectivity of protons over other ions in hHv1 channels.

Recently, notable progress has been made with the development of the multiscale reactive MD (MS-RMD) method (36), an MD approach that can in principle enable efficient, accurate, and transferable simulations of explicit proton transport (PT) involving amino acids and water chains ("wires") in complex biomolecular environments (37–39). Building upon these advances and the open-state model structure (32), we have performed extensive free energy sampling with MS-RMD for the PT process in the hHv1 channel as mediated by pore water molecules and the pore-lining Asp and Glu residues, without any prior bias toward a specific PT mechanism. Moreover, our investigations extend beyond PT and include a determination of the free energy profiles of cation and anion permeation through the channel. In turn, our calculations of proton and other ion permeabilities show good agreement with experimental measurements of ion selectivity and proton conductance, providing a quantitative picture of the proton selectivity mechanism. This work therefore provides a significant step toward unraveling the fundamental functional mechanism of voltage-gated proton channels.

Results and Discussion

Proton Permeation Mechanism in Wild-Type Hv1. We explored the unitary PT mechanism by mapping the explicit proton transport onto a two-dimensional (2D) free energy profile (the so-called potential of mean force or PMF) via 2D umbrella sampling (US). The reaction coordinates (RCs) used for the US (Fig. 1) include, first of all, the z coordinate of the charge defect associated with an excess proton (the so-called "center of excess charge" (40), abbreviated as CEC) relative to the protein center, denoted as Δz_H, (the cell membrane defines the xy-plane). This coordinate represents the overall PT process through the channel from the cytoplasm to the intra- and extracellular bulk compartments. The CEC definition is necessary because there is not just a single excess "proton" or hydronium cation when Grotthuss proton shuttling through water molecules and amino acids occurs, but instead, a dynamically changing net positive charge defect associated with there being one too many protons (an excess proton). However, many different protons on the water molecules and amino acids can contribute to shuttling that defect around. The second RC (Fig. 1) is the distance between the transporting protonic charge CEC and its closest pore-lining Asp/Glu residue, denoted as r_{min}. The second RC is crucial to differentiate whether the proton locally permeates the channel via titrating a protonatable amino acid residue (Fig. 1) or is mainly shuttling through the water molecules ("water wires").

The Fig. 2 *A* and *B* shows the PMF, also referred to as the free energy profile above, of the CEC as it traverses the inner pore of the hHv1 channel. (Note that hereafter this CEC may be referred to as "the proton.") The 2D PMF exhibits multiple deep wells situated around $r_{min} \approx 0$ Å, (cf. Fig. 2*A*, and more clearly highlighted in Fig. 2*B*). These wells correspond to the proton staying on the titratable residues (Asp/Glu) lining the pore. This observation

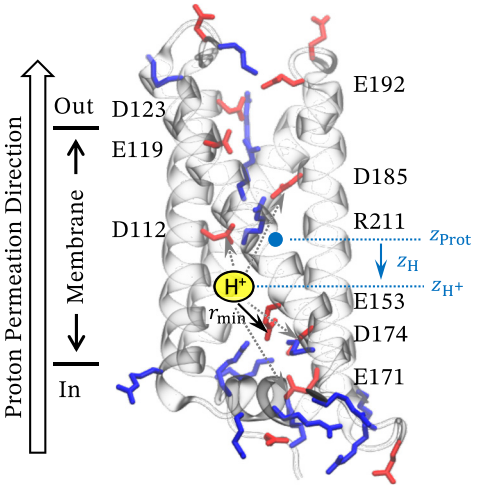

Fig. 1. Structural model of the WT conductive Hv1 channel. The charged pore-lining key residues to proton permeation are marked with residue ID (red: acidic; blue: basic). The direction of the proton permeation is from cytoplasmic to extracellular bulk water (marked by the arrow on the left). The reaction coordinate to describe the proton transport progress is defined as $\Delta z_H = z_{CEC} - z_{prot}$ (blue arrow), where z_{prot} is the z coordinate center of alpha carbons of the transmembrane Hv1 helices S1, S2, and S3, and z_{CEC} is the z coordinate of the center of excess charge. The reaction coordinate to distinguish the proton distance to the nearest acidic residues is defined as r_{min} (black arrow), which is a smoothed version of the minimum distance between the center of excess charge and all carboxyl oxygens of pore-lining Asp/Glu residues (dotted black arrows).

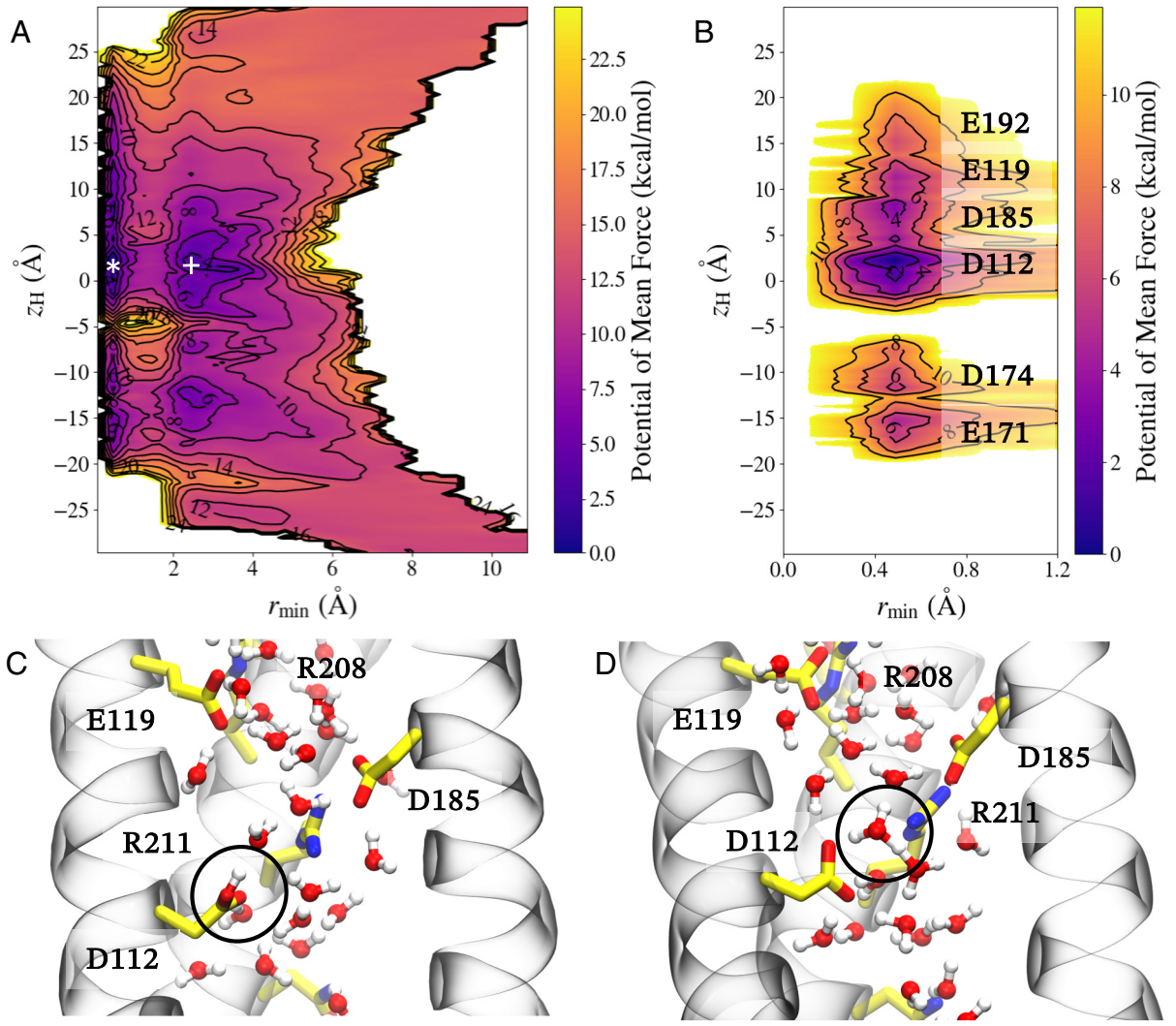

Fig. 2. Free energy profile of the proton permeation process in the wild-type hHv1 channel and representative molecular configurations. Panel *A*: The full free energy profile as a function of proton transport progress (z_H) and the proton distance to the closest protonatable residue (r_{min}). Panel *B*: A zoom-in of the free energy profile focusing on the states where proton resides on the pore-lining Asp/Glu residues. Panel *C*: A molecular configuration of the selective filter in D112 protonated state corresponding to the position of the "star" symbol in panel *A*. Panel *D*: A molecular configuration of the selective filter with solvated hydronium forming a contact ion pair with the deprotonated D112, corresponding to the "plus" symbol in panel *A*. The transported proton has been circled for clarity.

aligns with the results from a previous QM/MM metadynamics study (15) that observed spontaneous protonation events on pore-lining Asp/Glu residues. The free energy wells in the range of r_{min} from 2 Å to 4 Å correspond to instances where the proton resides in the first solvation shell of these titratable residues. Notably, these minimum wells are 3 to 4 kcal/mol less energetically favorable than the protonated wells of the corresponding residues, meaning that the purely water wire pathway is two orders of magnitude less likely to be observed than the pathway involving amino acid proton titrations, i.e., the proton transfer mechanism is most likely dominated by sequential proton hopping between the titratable Asp and Glu residues mediated by intervening water wires.

The selectivity filter region spanning from below residue D112 to above residue D185 corresponds to a relative vertical position along the channel, Δz_H, ranging from −5 Å to +10 Å. Notably, the global free energy minimum is associated with the excess proton residing on D112 (Fig. 2*C*), whereas the free energy minimum for the proton and D112 forming a contact ion pair (CIP, Fig. 2*D*) exhibits a higher free energy of ~3 kcal/mol. The 1D free energy profile (Fig. 3*A*), obtained by integrating the 2D PMF over the second reaction coordinate, r_{min}, shows the rate-limiting step of the full proton permeation process to be the dissociation of the proton from D112 to the extracellular bulk water, with the rate-limiting free energy barrier corresponding to the difference between an excess proton residing in bulk water and a proton in the D112 horizontal plane. In the wild-type (WT) channel, this free energy barrier is 12 kcal/mol, which is in reasonable agreement with the experimentally determined activation energy (41) (12.5 to 18.7 kcal/mol). Note that the activation energy does not reflect any entropic contribution, but the barrier free energy does. As such, the experimentally estimated activation barrier would be lower when considering the proton has higher entropic freedom at the barrier top due to a wider radius at the channel month compared to the narrow radius around D112 at the free energy minimum. It has been argued that the rate-limiting step of proton transport in hHv1 is the permeation through the channel based on 1) the weak pH dependence of the channel conductance (42) and 2) the high activation energy barrier reflected by the temperature sensitivity of the conductance (41). Our computations thus support this concept by directly revealing the high activation barrier corresponding to the proton dissociation from D112. The detailed proton selectivity mechanism associated with this proton

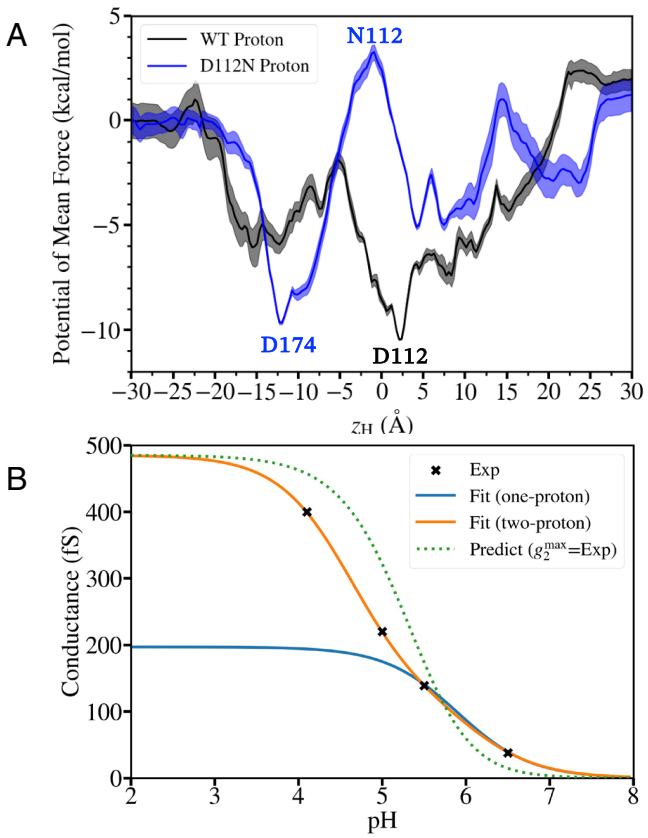

Fig. 3. Proton permeation free energy pathway in wild-type (WT) and mutant Hv1, with comparison to experimental conductance data. Panel *A*: One-dimensional free energy profile (PMF) for proton permeation in WT (black) and D112N mutant (blue) Hv1. Panel *B*: Comparison of calculated data and measured single channel conductance (43) under different pH conditions. The experimental data were fit with a one-proton model (blue solid) and a two-proton model (orange solid) as described in the text. The computationally predicted conductance curve with g_2^{max} obtained from the experimental fit is plotted with a dotted line.

permeation mechanism will be discussed in the next section along with the free energy profiles for other cation permeation.

Proton Permeation Mechanism in the D112N hHv1 Mutant. Electrophysiological experiments have revealed that the D112N mutation abolishes proton selectivity and exhibits anion permeation (13), but an explanation for how a single site mutation can shift a proton channel into an anion-selective channel is still elusive. As a first step in understanding the anion versus proton selectivity, we examined the PT mechanism in the D112N mutant channel by calculating the 2D PMF adopting the same reaction coordinates as were used in the WT free energy sampling. As shown in *SI Appendix*, Fig. S1 of Supplemental Material, the most likely PT pathway remains the proton hopping between protonatable residues mediated by water wires, while D112, being mutated to asparagine, loses its reactive capability to bind a proton, and thus the proton can only permeate through the SF via water wires. In addition, the mutation switches the total charge of selectivity filter residues (D112 to N112, D185, and R221) from negative to neutral, and as a result, a large free energy barrier is now seen in the proton 1D PMF (Fig. 3*A*), even before the proton reaches the selectivity filter region ($\Delta z_H = 0$Å). Notably, the global free energy minimum is shifted to the position of D174. This implies that in the case of a low cytoplasmic pH, a two-proton knock-on permeation mechanism may occur in WT hHv1 if we regard the D112N channel as mimicking the D112 protonated state of the WT channel.

pH-Dependent Proton Conductance of hHv1. Cherny et al. (43) measured the unitary proton conductance (the conductance of a single channel when it is open; thus not reflecting the pH-dependent gating but instead the proton permeation itself) under various pH conditions (summarized in Fig. 3*B*). To understand the origin of the pH dependence, we first fit the experimental data with a two-proton conduction model as follows:

$$g_2(c) = \frac{cK_1 g_1^{\max}}{1^\circ + cK_1 + c^2K_1K_2} + \frac{c^2K_1K_2 g_2^{\max}}{1^\circ + cK_1 + c^2K_1K_2}, \quad [1]$$

where $c = 10^{-p\mathrm{H}}$ is the proton concentration, $g_2(c)$ is the conductance value as the function of proton concentration, and K_1 and K_2 are the binding constants of a single proton and a second proton to the protein, respectively. The terms $g_1^{\max}$ and $g_2^{\max}$ are the saturated maximum conductance for a one-proton and for a two-proton mechanism accordingly. In Eqs. **1** and **2**, we assume that the pH dependence of conductance arises from the pH-dependent probabilities of the channel being in a single-proton-bound or a two-proton-bound state, and the total conductance is thus the weighted average of the two conduction mechanisms. The fitted curve is shown in Fig. 3*B* and the fitted parameters are listed in Table 1. When the two-proton mechanism is disregarded, the model simplifies to a single-proton conductance model, given by

$$g_1(c) = \frac{cK_1 g_1^{max}}{1^\circ + cK_1}, \quad [2]$$

which coincides with Levitt's derivation (44) using the Nernst–Planck equation, assuming a channel only allows one single ion to permeate at the same time. Such a single-proton model, however, does not describe the data over the entire pH range tested (blue solid curve in Fig. 3*B*). As such, the two-proton model represents the minimal model that fits the measured conductance at various pH levels. The need for such a two-proton model is in line with our analysis of the PT PMF of the mutant channel. As discussed earlier, the deep free energy well observed at the position of D174 in the D112N mutant—a state that mimics the protonated D112 state of the WT channel—suggests a second proton binds to D174 in WT following the titration of D112. This observation, along with the need for a two-proton model to better fit the experimental data, points to a two-proton knock-on mechanism involving D174 and D112 as the two key protonation sites under acidic pH conditions.

The proton permeation PMFs allow us to directly compute the one-proton binding constant K_1 and, combined with the Nernst–Planck equation, also the one-proton maximum conductance $g_1^{\max}$ (*SI Appendix*, Supplementary Material). The second

Table 1. Conductance model parameters*

	$g_1^{\max}$(fS)	pK_{d1}	$g_2^{\max}$(fS)	pK_{d2}
Comp.	21.7 ± 8.6	6.4 ± 0.2	–	5.3 ± 0.2
Exp. Fit	131	6.1	485	4.6

*The symbols $g_1^{\max}$ and $g_2^{\max}$ stand for the maximum conductance of one-proton and two-proton mechanisms, respectively. K_{d1} and K_{d2} stand for the proton disassociation constant from the protein. The fitted experimental parameters of the one-proton and two-proton conducting model were obtained by fitting Eqs. **1** and **2** against the experimental conductance measurements. The computational parameters were obtained from proton permeation PMFs and diffusion constants. Details can be found in *Methods* and *SI Appendix, Supplementary Material*.

proton binding constant K_2 represents the binding affinity of hHv1 to a second proton given that a proton already resides in the channel. Since D112 is the global minimum in the WT PMF, it is the most probable protonation site for the first incoming proton. As noted earlier, assuming the D112N mutant mimics the one-proton-bound state of WT, K_2 can be estimated as the single proton affinity for the D112N channel. Table 1 presents the agreement between our calculated K_1, K_2, and g_1^{max} and the experimentally fitted data, thus providing a degree of validation for our proton transport free energy calculations. The agreement is well within an order of magnitude, which is a degree of accuracy very difficult to obtain from molecular-level simulation of a system this complicated.

The second-proton maximum conductance g_2^{max} corresponding to the knock-on mechanism cannot be directly obtained from our present calculations, but it can be approximated by considering the deprotonation timescale of D112 to the bulk when D174 remains protonated. Considering that D174, located beneath D112, is charge neutral when it is protonated, it is expected that the deprotonated barrier for a proton to leave D112 would be lower compared to the case in WT with a negatively charged D174. Consequently, the transport rate of such a knock-on mechanism is anticipated to be faster than that of a single proton mechanism. This expectation is consistent with the observation that the fitted g_2^{max} is larger than the fitted g_1^{max}. Given our computed K_1, K_2, and g_1^{max}, together with the experimentally fitted g_2^{max}, we plotted the pH-dependent conductance in Fig. 3*B* (green dotted curve), which shows reasonable agreement with the experimentally determined one.

Proton Selectivity to TMA^+ Cation in WT Hv1. The central quantity governing selectivity is the ion permeability through the channel. The selectivity can be reflected from a comparison between ions' Nernst potential and the experimentally measured V_{rev} based on the Goldman–Hodgkin–Katz (GHK) voltage equation (45, 46),

$$V_{rev} = \frac{RT}{zF}\log\frac{P_{CH_3SO_3^-}\left[CH_3SO_3^-\right]_i + P_{OH^-}[OH^-]_i + P_{H^+}\left[H^+\right]_o + P_{TMA^+}\left[TMA^+\right]_o}{P_{CH_3SO_3^-}\left[CH_3SO_3^-\right]_o + P_{OH^-}[OH^-]_o + P_{H^+}\left[H^+\right]_i + P_{TMA^+}\left[TMA^+\right]_i}, \quad [3]$$

where R is the ideal gas constant, T is the temperature in Kelvin, F is Faraday's constant, z is the charge of the ions (here, $z = 1$ for monovalent ions), and P is the permeabilities of certain ions. The GHK equation establishes a framework for the competition among potentially permeant ions to determine V_{rev}. Each ion shifts V_{rev} toward its respective Nernst potential, and the observed $V_{rev} = V_H$ for WT hHv1 can be attributed to the dominant contribution from protons, expressed as the product of its permeability and bulk concentration largely surpassing the ones of other ions.

Several studies (13, 42, 47–49) have conducted electrophysiological measurements to investigate the selectivity of protons over the tetramethylammonium cation (TMA^+). The proton-to-TMA^+ permeability ratio determined from the measured V_{rev} using the GHK equation consistently yields $P_{H^+}/P_{TMA^+} >> 1.0 \times 10^7$. Like the proton permeation PMF calculations, we ran umbrella sampling using the z-coordinate of the nitrogen atom of TMA^+ relative to the protein center, Δz_{TMA}, as the permeation coordinate to quantify the cation permeation free energy profile. In contrast to the excess proton, TMA^+ cations are unable to bind to D112 and their larger radius makes it unfavorable for them to reside within the narrow region of the selectivity filter. Consequently, TMA^+ cations tend to be more stable below the selective filter region rather than inside it, as indicated by the presence of a free energy well below $\Delta z_{TMA} = 0$Å (Fig. 4*A*).

The ion permeability can be calculated as (50–52)

$$P_{ion} = k_1 \int_{Protein} d\Delta z e^{-\beta(W(\Delta z) - W(\Delta z_0))} \propto k_1 K_1, \quad [4]$$

where $W(\Delta z)$ is the 1D PMF for ion permeation, and $W(\Delta z_0)$ is its value when reaching a plateau in the bulk region. The integral was performed over the transmembrane protein region. k_1 is the rate constant of a single ion permeating through the channel, and K_1 is its first-order binding constant of the given ion to the protein (*Methods* for detailed expressions for k_1 and K_1). The calculated permeability ratio between a proton and a TMA cation is 1.4×10^7, in good agreement with the experimentally estimated lower bound (1×10^7). We note that due to the imperfect control of pH in some experimental measurements, this number is a conservative estimate while the true number may be larger. Since our calculated proton conductance and proton binding affinity are in good agreement with experimental data (Table 1), and the proton permeability is unambiguously determined by these two numbers, we suggest that our calculated TMA permeability is an overestimate. Such a deviation may be attributed to the lack of electronic polarizability of the ion solvation environment described by classical force fields, partially supported by the subtle dependence on the water model in the TMA free energy profile (*SI Appendix*, Fig. S3). The MS-RMD approach, conversely, explicitly polarizes the proton solvation waters up to the third solvation shell.

By expressing permeability as the product of the rate constant and the binding constant, we can interpret this quantity as the combination of an ion's probability of being inside the channel (binding constant, determined by the depth of the free energy well) and the rate at which the ion can pass through the channel (transport rate constant, influenced by the free energy barrier and its diffusion constant). Notably, in this perspective the origin of proton selectivity, i.e., the large permeability ratio between the proton and TMA comes from the tighter binding of protons ($K_1(H^+) = 10^{6.4\pm0.2} \gg K_1(TMA^+) = 10^{-0.4\pm0.3}$), instead of the transport rate constant ($k_1(H^+) = 3.5 \pm 0.7 \times 10^3\ s^{-1} \approx k_1(TMA^+) = 1.2 \pm 0.6 \times 10^3\ s^{-1}$). This finding contradicts a typical expectation regarding a selectivity filter to restrict the movement of ions other than the selected ion, resulting in a noticeable distinction in the transport rate and/or the rate-limiting free energy barrier. For example, the tighter binding of K^+ over Na^+ to the voltage-gated potassium channel from *Streptomyces lividans* (53) (KcsA) lowers the transport free energy barrier by 4 to 5 kcal/mol (54–56), resulting in several orders of difference in the transport rate constant. Another example is the Outer Membrane Protein F from *Escherichia coli* (57) (OmpF) whose wide inner pore favors conduction of a broad range of cations over anions. A comparison of free energy and diffusion constant profiles of K^+ and Cl^- permeation (57) has revealed large contributions from transport rate differences to the cation selectivity. The key difference from the hHv1 channel lies in the shape of the permeation free energy profile. In these channels mentioned above, the PMF of ion permeation reaches a peak inside the channel and thus, tighter binding reduces the barrier and increases the transport rate. In hHv1, however, the proton PMF reaches a global minimum inside the channel, meaning that tighter binding results in larger free energy cost when leaving the channel and thus reduces the transport rate. Apparently, the hHv1

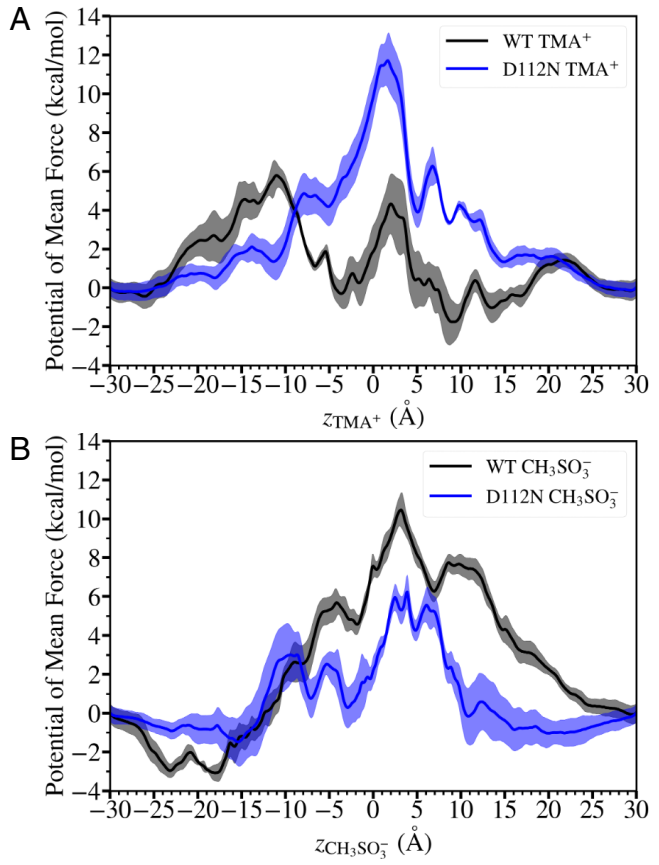

Fig. 4. The ion permeation PMFs. Panel *A*: Permeation PMFs of TMA^+ cation in wild-type (WT, black) and D112N mutant (blue). Panel *B*: Permeation PMFs of $CH_3SO_3^-$.

channel sacrifices its proton transport capability for a strong proton binding affinity. This strategy enables the channel to accumulate protons that are scarce in solution at the physiological pH, and when interpreting the binding constant $K_1 = 10^{6.4}$ as the accumulating factor, the channel increases the local concentration of protons by six orders of magnitude from the bulk concentration. The distinct behavior of hHv1 can be explained by the unique properties of proton permeation involving the titration events of pore-lining residues. The association and dissociation of protons require a much larger free energy change compared to ion association; as a result, the free energy profile for proton permeation has a much deeper free energy well compared to that for ion transport. This deep free energy well is reminiscent of the observed well at the titratable residues (58, 59) H37 in the influenza A M2 channel, suggesting a similar proton selectivity mechanism in M2, but further calculations of the transport free energy of other ions in M2 are needed to confirm this hypothesis. In contrast, a de novo designed proton channel (60) may exhibit a more "conventional" selectivity mechanism, where the difference in permeation rate plays a dominant role in determining selectivity, due to the absence of proton binding residues (Table 2).

Table 2. The proton permeability ratio compared to TMA^+ and $CH_3SO_3^-$

	WT	D112N mutant
P_{H^+}/P_{TMA^+}	1.4×10^{7}	1.9×10^{7}
$P_{H^+}/P_{CH_3SO_3^-}$	3×10^{10}	7.1×10^{3}

The significant influence of binding affinity on proton permeability also emphasizes the unique nature of D112 among other pore-lining reactive residues. The protonated D112 serves as the global minimum in the free energy landscape (Fig. 2*A*), contributing the most to the binding affinity of the excess proton. This distinctive function of D112 draws support from the experimental observations that neutralizing single-site mutations of residue D185 and D174 still maintain proton selectivity (13, 61), as they exhibit weaker proton-binding properties compared to D112 in hHv1.

Anion Selectivity in D112N Hv1 Mutant. As discussed earlier, electrophysiological experiments (13) revealed the D112N mutant as an anion channel, transporting both $CH_3SO_3^-$ and Cl^-. This was seen by the positive shift in the V_{rev} value when all types of ions (except H^+ and OH^-) were diluted with sucrose in the extracellular solution. A negative shift in the V_{rev} value, however, was observed when the extracellular pH (pH_o) was adjusted from 5.5 to 7.0, suggesting considerable permeation of either protons, hydroxide, or both, at a comparable level to anions. The sucrose effect being greater at pH_o 5.5 than 7.0 indicates OH^- instead of H^+ to be a dominant permeating ion in the D112N mutant, but this does not eliminate the possibility of proton as one of the current carriers.

To address these uncertainties, we also conducted umbrella sampling to examine the permeation free energies of TMA^+ and $CH_3SO_3^-$ in the D112N mutant. Fig. 4 indicates that the anion could be stabilized below the selective filter (D185 and R211), evidenced by the free energy well around $\Delta z_{CH_3SO_3^-} = -3$Å (Fig. 4*B*), whereas the cation could not. Compared to the permeation free energies in the WT channel, the barrier for TMA^+ transport was increased by the mutation, and the barrier for $CH_3SO_3^-$ was greatly reduced. This discrepancy can be attributed to the electrostatic effect in the D112N mutant, where the arginine residue is positioned closer to the base of the selective filter.

Permeability calculations revealed that the permeability ratio of protons to $CH_3SO_3^-$ is $P_{H^+}/P_{CH_3SO_3^-} = 7.1\times10^3$, and the ratio of TMA^+ to $CH_3SO_3^-$ is $P_{TMA^+}/P_{CH_3SO_3^-} = 3.7\times10^{-4}$. The significant drop in $P_{TMA^+}/P_{CH_3SO_3^-}$ ratio compared to the WT counterpart reveals the loss of proton selectivity over anions and suggests OH^- permeation contributing to the V_{rev} shift when changing the external pH. Although the D112N mutant loses its proton selectivity over anions, it is interesting to note that the channel continues to exhibit proton selectivity over the TMA^+ cation, as indicated by a permeability ratio of $P_{H^+}/P_{TMA^+} = 2.0\times10^7$. To further confirm the OH^- preference, we fit the permeability of OH^- using the GHK equation (Eq. **3**) to the experimentally measured −12.5 mV V_{rev} shift (13) when pH_o changes from 5.5 to 7.0 while keeping the internal pH (pH_i) fixed at 5.5 (note the only species with unknown permeability value in Eq. **3** is the OH^- ion). We obtained $P_{OH^-}/P_{H^+} = 52$, indeed showing the preference of OH^-. We validated the obtained permeability ratios, including the ones from PMFs using Eq. **4**, along with the fitted ratio P_{OH^-}/P_{H^+} by computing the V_{rev} shifts due to sucrose dilution at different pH_o conditions. The computed shifts due to external ion concentration reduction by 10 times are 32 mV and 20 mV at pH_o = 5.5 and pH_o = 7, in reasonable agreement with the experimentally measured values (~40 mV and ~20 mV according to figure 3E of ref. 13). Given these permeability ratios and considering the physiological pH (10^{-7} M) and anion concentration (0.15 M), the contribution of $P_{CH_3SO_3^-}[CH_3SO_3^-]$ and $P_{OH^-}[OH^-]$ to the GHK equation are comparable, so the broad-spectrum

anion-selective nature of the mutant channel under these conditions is thus confirmed.

Although the permeability ratios of OH^- over H^+ cation and $[CH_3SO_3^-]$ over H^+ undoubtedly show an anion preference, none of these numbers are infinite, meaning that the D112N mutant channel may exhibit proton selectivity under certain conditions. According to the GHK equation, we predict the D112N channel restores the proton selectivity at around pH = 4 and low ion concentration (~10 mM). This may be validated by measuring V_{rev} shift when changing from $pH_i = 3/pH_o = 3$ to $pH_i = 3/pH_o = 4.5$ in a bath of 10 mM of $[CH_3SO_3^-]$, and comparing to the proton Nernst potential (–87 mV).

Conclusions

This study has employed extensive reactive MD simulations and free energy sampling to elucidate the origins of selectivity and permeability for protons and other ions through the hHv1 channel.

The analysis provides the free energy profile for proton permeation, thus highlighting the role of key acidic residues while calling into question the plausibility of a purely water-wire conduction mechanism. Using a two-proton conduction model, the proton conductance was quantitatively analyzed for the wild-type channel under different pH conditions. Additionally, ion selectivity among protons, TMA, and methanesulfonate was examined in the wild type as well as in the D112N mutant, the latter being known to exhibit anion permeation.

It was found that the extraordinary proton selectivity of the wild-type channel is primarily due to its strong proton affinity, rather than to a lower proton transport free energy barrier. This contrasts with several other selective ion channels where kinetic blocking effects are significantly more pronounced for species other than the selectively transported ion. It was further shown that the D112N substitution induces electrostatic alterations that disrupt proton conductance, allowing for substantial anion leakage and a possible preference for OH^- to be transported over H^+.

Methods

Classical Molecular Dynamics Equilibration (Classical MD). Starting from the conductive wild-type Hv1 structure (32), we performed classical MD equilibration for 2 microseconds with protonation states of the protein assigned as in neutral pH condition according to pKa predictions by PROPKA (62) on the starting structure. The protein was embedded in a pre-equilibrated and hydrated 1-Palmitoyl-2-oleoyl-sn-glycero-3-phosphocholine (POPC) lipid bilayer with approximately 150 mM of NaCl under a constant external electric field of 0.0156 V/nm on the z axis to simulate the conductive Hv1 channel under a +150 mV depolarized membrane potential. All interactions were described by the CHARMM36 force field (63) with CMAP correction and the TIP3P water model. Models were built and equilibrated using a standard protocol in CHARMM-GUI (64) and simulations were performed in GROMACS (65, 66) version 2020.4 with the Velocity Verlet integrator using a time step of 2 fs in the isothermal–isobaric [constant particle Number, Pressure, Temperature (NPT)] ensemble using a semi-isotropic Parrinello–Rahman barostat (67) at 1 atm and a velocity rescaling thermostat (68) (300 K). The same equilibration procedure was carried out in parallel for the D112N mutant. Electrostatic interactions were calculated using the particle mesh Ewald method with a cutoff of 12.0 Å and a precision of 10-5 was used to treat the electrostatic interactions. The Lennard-Jones (LJ) interaction was set to cutoff to 0 at a 12.0 Å radius and used a switching function starting at 10.0 Å to smooth the truncation. All bonds involving hydrogens were constrained using the LINCS algorithm (69).

Multiscale Reactive Molecular Dynamics (MS-RMD) Simulations. Starting from the equilibrated conductive Hv1 structure of both wild-type and D112N mutant in classical MD, the MS-RMD simulations were performed to simulate the explicit proton permeation process with all pore-lining Glu/Asp residues modeled as potential protonation sites while one additional excess proton was added to a pore-water replacing a Na^+ in the bulk. All interactions were described by the CHARMM36 force field with CMAP correction with the previously developed Asp and Glu MS-RMD models (37, 38). Simulations were performed by LAMMPS MD package (70) coupled with RAPTOR (36) for proton reactions. The MD was integrated with a time step set to 1 fs in the canonical [constant particle Number, Volume, Temperature (NVT)] ensemble using a Nose–Hoover chain thermostat at 300 K and with an orthogonal box of previously equilibrated dimension (77.493 Å, 77.483 Å, 99.581 Å) for WT Hv1 and (77.471 Å, 77.471 Å, 99.587 Å) for the D112N mutant. Electrostatic interactions were calculated using the particle–mesh Ewald method with the relative RMS error in per-atom forces calculated by the long-range solver, with the reference force of the two unit point charges (e.g., ref. 2 monovalent ions) exerted on each other at a distance of 1 Å, to be less than 10^{-4}. The Lennard-Jones (LJ) and Coulombic interactions was set to cutoff to 0 at 10.0 Å radius and used a switching function starting at 8.0 Å to smooth the truncation.

2-Dimensional umbrella sampling with MS-RMD simulations. To enhance the sampling of the free energy landscape of proton permeation through the channel, two-dimensional umbrella sampling of the two coordinates describing the "reaction" (the collective variables, CVs) was performed by the PLUMED2 package (71) incorporated with LAMMPS/RAPTOR. The principal reaction coordinate CV was defined as

$$\Delta z_H = z_{CEC} - z_{Prot}, \quad [5]$$

where CEC is the center of excess charge described earlier, i.e., a virtual "particle" mathematically defined to track the position of the net positive charge defect associated with the transporting excess protons as they shuttle through water molecules and protonatable amino acids. The subscript Prot in Eq. **5** stands for the geometric center of alpha carbons of the transmembrane Hv1 helices S1, S2, and S3, defined as residues 103 to 122, 138 to 160, and 172 to 188. The second reaction coordinate CV was defined as a smooth and differentiable version of the minimum distance,

$$r_{min} = \frac{\beta}{\log\left[\sum_i \exp\left(\frac{\beta}{s_i}\right)\right]}, \quad [6]$$

where the β parameter is set to be 90 Å, and s_i is the distance between the i-th carboxyl oxygen of all pore-lining Asp/Glu residues and the transported excess proton CEC.

To restrain the lateral diffusion of the hydrated proton when completely dissociated from the protein, a flat-bottom cylinder potential (72) was introduced to the reaction coordinate $\sqrt{r_\perp}$ defined as the radial distance of the transported proton to the center of protein.

$$r_\perp = \sqrt{(x_{CEC} - x_{Prot})^2 + (y_{CEC} - y_{Prot})^2}. \quad [7]$$

The force constant of the wall was set to 5 kcal/mol/Å^2, and the restraining potential was switched on once $r_\perp \geq 7$Å in umbrella windows where $|\Delta z_H| \geq 26$Å.

A total of over 1,500 umbrella windows were established for 2D umbrella sampling in the WT and D112N Hv1 systems, with a spacing of 0.5 Å in both the Δz_H and r_{min} dimensions. Each umbrella window was run for ~1 ns and the total simulation time exceeded 1 μs. The weighted histogram analysis method (73) (WHAM) was employed to combine the 2D umbrella sampling data and calculate the 2D PMF. The 1D PMF as a function of Δz_H was obtained from integration of the 2D PMF over the r_{min} dimension. The PMF error bars were obtained by partitioning the trajectories of all umbrella windows into six equally sized blocks and calculating the SD using the last five blocks.

Replica Exchange Umbrella Sampling with Classical Simulations. To enhance the sampling of free energy landscape of TMA^+ and $CH_3SO_3^-$ ion permeation through the channel, replica exchange umbrella sampling on the reaction coordinate z_{ion} was performed with the PLUMED2 package (71) incorporated with GROMACS (65, 66). The reaction coordinate was defined as

$$\Delta z_{ion} = z_{Ion} - z_{Prot}, \quad [8]$$

where Ion represents the center nitrogen atom of the TMA^+ cation or the center sulfur atom of the $CH_3SO_3^-$ anion. Prot adopted the same definition of protein center when defining Δz_H in the 2D proton umbrella sampling. To restrain the lateral diffusion of the transported ion when completely dissociated from protein, we employed a similar cylindrical restraint on $r_\perp$ with a force constant of 10 kcal/mol/Å^2. The timestep for each classical simulation was set to 2 fs and adjacent umbrella windows attempted to exchange every 10 ps. Umbrella windows were set for a spacing of 0.5 Å and the force constant of each umbrella potential was set to 5 kcal/mol/Å^2. More than 125 umbrella windows were set, and each umbrella window was run for ~10 ns with a total simulation time exceeding 1 μs for both WT Hv1 and D112N mutant systems. We utilized the SPC/E water model (74) to enable a more direct comparison with the MS-RMD simulations, which uses the SPC/Fw as the water model (75). *SI Appendix*, Fig. S3 shows how results are dependent on the water model. WHAM was employed to combine the umbrella sampling data and calculate the 1D PMF. The PMF error bars were obtained by partitioning the trajectories of all replica-exchanged umbrella windows into six equally sized blocks and calculating the SD using the last five blocks.

Permeability calculation. The ion dissociation constant can be calculated from the expression (76) below.

$$pK_d = \lg c_0 xV = \lg c_0 \int_{\text{Protein}} d\Delta z e^{-\beta\left(W(\Delta z)-W(\Delta z_0)\right)} \int_0^{+\infty} 2\pi r e^{-\beta U^{\text{bias}}(r_\perp,\Delta z_0)} dr_\perp. \quad [9]$$

Here, $c_0 = 1/1660$ Å^{-3} is the standard state concentration (1 M) expressed in number density, $W(\Delta z)$ is the 1D PMF of ion permeation, and $W\left(\Delta z_0\right)$ is its value when reaching a plateau in the bulk region. The term $U^{\text{bias}}\left(r_\perp, \Delta z_0\right)$ is the cylindrical restraint potential used in the umbrella windows, note here that the cylinder potential is a flat-bottom-shaped potential that is only turned on when the transported ion is outside the cylinder region. The integral was performed over the transmembrane protein region defined as $-22\text{Å} \le \Delta z \le +22\text{Å}$. The binding constant is related to the dissociation constant via $K_b = 10^{pK_d}$. The permeabilities were obtained separately from the PMFs of each block and calculating the SE using the last five blocks out of six blocks.

The transport rate constant can be calculated from the Nernst–Planck equation (44) in terms of a 1D PMF, as

$$k = \frac{1}{\left(\int_{\text{Protein}} d\Delta z \exp - \beta W(\Delta z)\right)\left(\int_{\text{Protein}} d\Delta z \frac{\exp \beta W(\Delta z)}{D(\Delta z)}\right)}, \quad [10]$$

where $D(\Delta z)$ is the position-dependent diffusion constant. A comparison to an alternative, the Markov state model (MSM) approach to compute the transport rate, can be found in *SI Appendix, Supplementary Computational Details*.

Data, Materials, and Software Availability. All study data are included in the article and/or *SI Appendix*.

ACKNOWLEDGMENTS. This research was supported in part by the National Institute of General Medical Sciences (NIGMS) of the NIH through grants R01GM053148 to G.A.V and R01GM098973 to D.J.T. The content is solely the responsibility of the authors and does not necessarily represent the official views of the NIH. The research was also supported in part by the Camille and Henry Dreyfus Foundation (Grant ML-22-148 to G.A.V) and by the Office of Naval Research (Award N00014-21-1-2157 to G.A.V.). Computing resources were provided by the Extreme Science and Engineering Discovery Environment (XSEDE), which is supported by NSF Grant OCI-1053575, and by the University of Chicago Research Computing Center (RCC). We thank Prof. Thomas Decoursey of Rush University and Dr. Yuxing Peng of NVIDIA for fruitful discussions on Hv1.

1. T. E. Decoursey, Voltage-gated proton channels and other proton transfer pathways. *Physiol. Rev.* **83**, 475–579 (2003).
2. T. E. DeCoursey, Transcendent aspects of proton channels. *Annu. Rev. Physiol.* **86** (2024).
3. I. S. Ramsey, E. Ruchti, J. S. Kaczmarek, D. E. Clapham, Hv1 proton channels are required for high-level NADPH oxidase-dependent superoxide production during the phagocyte respiratory burst. *Proc. Natl. Acad. Sci. U.S.A.* **106**, 7642–7647 (2009).
4. T. Schilling, A. Gratopp, T. E. DeCoursey, C. Eder, Voltage-activated proton currents in human lymphocytes. *J. Physiol.* **545**, 93–105 (2002).
5. L.-J. Wu, Voltage-gated proton channel HV1 in microglia. *Neuroscientist* **20**, 599–609 (2014).
6. R. Zhao *et al.*, Role of human Hv1 channels in sperm capacitation and white blood cell respiratory burst established by a designed peptide inhibitor. *Proc. Natl. Acad. Sci. U.S.A.* **115**, E11847–E11856 (2018).
7. R. Zhao *et al.*, Direct activation of the proton channel by albumin leads to human sperm capacitation and sustained release of inflammatory mediators by neutrophils. *Nat. Commun.* **12**, 3855 (2021).
8. Y. Wang *et al.*, Specific expression of the human voltage-gated proton channel Hv1 in highly metastatic breast cancer cells, promotes tumor progression and metastasis. *Biochem. Biophys. Res. Commun.* **412**, 353–359 (2011).
9. Y. Wang, X. Wu, Q. Li, S. Zhang, S. J. Li, Human voltage-gated proton channel Hv1: A new potential biomarker for diagnosis and prognosis of colorectal cancer. *PLOS One* **8**, e70550 (2013).
10. L. Ribeiro-Silva, F. O. Queiroz, A. M. B. da Silva, A. E. Hirata, M. Arcisio-Miranda, Voltage-gated proton channel in human glioblastoma multiforme cells. *ACS Chem. Neurosci.* **7**, 864–869 (2016).
11. T. E. DeCoursey, The voltage-gated proton channel: A riddle, wrapped in a mystery, inside an enigma. *Biochemistry* **54**, 3250–3268 (2015).
12. T. E. DeCoursey, Voltage-gated proton channels: molecular biology, physiology, and pathophysiology of the HV family. *Physiol. Rev.* **93**, 599–652 (2013).
13. B. Musset *et al.*, Aspartate 112 is the selectivity filter of the human voltage-gated proton channel. *Nature* **480**, 273–277 (2011).
14. T. Dudev *et al.*, Selectivity Mechanism of the Voltage-gated Proton Channel, HV1. *Sci. Rep.* **5**, 10320 (2015).
15. S. C. van Keulen *et al.*, Does proton conduction in the voltage-gated H+ channel hHv1 involve Grotthuss-like hopping via acidic residues?. *J. Phys. Chem. B* **121**, 3340–3351 (2017).
16. M. Lee, C. Bai, M. Feliks, R. Alhadeff, A. Warshel, On the control of the proton current in the voltage-gated proton channel Hv1. *Proc. Natl. Acad. Sci. U.S.A.* **115**, 10321–10326 (2018).
17. I. S. Ramsey *et al.*, An aqueous H+ permeation pathway in the voltage-gated proton channel Hv1. *Nat. Struct. Mol. Biol.* **17**, 869–875 (2010).
18. M. L. Wood *et al.*, Water wires in atomistic models of the Hv1 proton channel. *Biochim. Biophys. Acta (BBA).* **1818**, 286–293 (2012).
19. A. L. Bennett, I. S. Ramsey, CrossTalk opposing view: Proton transfer in Hv1 utilizes a water wire, and does not require transient protonation of a conserved aspartate in the S1 transmembrane helix. *J. Physiol.* **595**, 6797 (2017).
20. T. Lazaridis, Proton Paths in Models of the Hv1 Proton Channel. *J. Phys. Chem. B* **127**, 7937–7945 (2023).
21. K. Kulleperuma *et al.*, Construction and validation of a homology model of the human voltage-gated proton channel hHV1. *J. General Physiol.* **141**, 445–465 (2013).
22. A. Chamberlin *et al.*, Hydrophobic plug functions as a gate in voltage-gated proton channels. *Proc. Natl. Acad. Sci. U.S.A.* **111**, E273–E282 (2014).
23. Y. Peng, J. M. J. Swanson, S.-G. Kang, R. Zhou, G. A. Voth, Hydrated excess protons can create their own water wires. *J. Phys. Chem. B* **119**, 9212–9218 (2015).
24. S. Lee, H. B. Mayes, J. M. J. Swanson, G. A. Voth, The origin of coupled chloride and proton transport in a Cl–/H+ antiporter *J. Am. Chem. Soc.* **138**, 14923–14930 (2016).
25. R. Liang, J. M. J. Swanson, Y. Peng, M. Wikström, G. A. Voth, Multiscale simulations reveal key features of the proton-pumping mechanism in cytochrome c oxidase. *Proc. Natl. Acad. Sci. U.S.A.* **113**, 7420–7425 (2016).
26. Z. Wang, J. M. J. Swanson, G. A. Voth, Modulating the chemical transport properties of a transmembrane antiporter via alternative anion flux. *J. Am. Chem. Soc.* **140**, 16535–16543 (2018).
27. C. Li, G. A. Voth, A quantitative paradigm for water-assisted proton transport through proteins and other confined spaces. *Proc. Natl. Acad. Sci. U.S.A.* **118**, e2113141118 (2021).
28. K. Takeshita *et al.*, X-ray crystal structure of voltage-gated proton channel. *Nat. Struct. Mol. Biol.* **21**, 352–357 (2014).
29. Q. Li *et al.*, Resting state of the human proton channel dimer in a lipid bilayer. *Proc. Natl. Acad. Sci. U.S.A.* **112**, E5926–E5935 (2015).
30. M. Bayrhuber *et al.*, Nuclear magnetic resonance solution structure and functional behavior of the human proton channel. *Biochemistry* **58**, 4017–4027 (2019).
31. D. E. Shaw *et al.*, Anton, a special-purpose machine for molecular dynamics simulation. *Commun. ACM* **51**, 91–97 (2008).
32. A. D. Geragotelis *et al.*, Voltage-dependent structural models of the human Hv1 proton channel from long-timescale molecular dynamics simulations. *Proc. Natl. Acad. Sci. U.S.A.* **117**, 13490 (2020).
33. V. T. Lim, J. A. Freites, F. Tombola, D. J. Tobias, Thermodynamics and Mechanism of the Membrane Permeation of Hv1 Channel Blockers. *J. Membrane Biol.* **254**, 5–16 (2021).
34. V. T. Lim *et al.*, Insights on small molecule binding to the Hv1 proton channel from free energy calculations with molecular dynamics simulations. *Sci. Rep.* **10**, 13587 (2020).
35. C. Zhao *et al.*, A novel Hv1 inhibitor reveals a new mechanism of inhibition of a voltage-sensing domain. *J. General Physiol.* **153**, e202012833 (2021).
36. T. Yamashita, Y. Peng, C. Knight, G. A. Voth, Computationally efficient multiconfigurational reactive molecular dynamics. *J. Chem. Theory Comput.* **8**, 4863–4875 (2012).
37. C. Li, G. A. Voth, Accurate and transferable reactive molecular dynamics models from constrained density functional theory. *J. Phys. Chem. B* **125**, 10471–10480 (2021).
38. J. Zuchniarz, Y. Liu, C. Li, G. A. Voth, Accurate pKa calculations in proteins with reactive molecular dynamics provide physical insight into the electrostatic origins of their values. *J. Phys. Chem. B* **126**, 7321–7330 (2022).
39. C. Li, Z. Yue, S. Newstead, G. A. Voth, Proton coupling and the multiscale kinetic mechanism of a peptide transporter. *Biophys. J.* **121**, 2266–2278 (2022).
40. C. M. Maupin, K. F. Wong, A. V. Soudackov, S. Kim, G. A. Voth, A multistate empirical valence bond description of protonatable amino acids. *J. Phys. Chem. A* **110**, 631–639 (2006).
41. T. E. DeCoursey, V. V. Cherny, Temperature dependence of voltage-gated H+ currents in human neutrophils, rat alveolar epithelial cells, and mammalian phagocytes *J. General Physiol.* **112**, 503–522 (1998).
42. V. V. Cherny, V. S. Markin, T. E. DeCoursey, The voltage-activated hydrogen ion conductance in rat alveolar epithelial cells is determined by the pH gradient. *J. General Physiol.* **105**, 861–896 (1995).
43. V. V. Cherny, R. Murphy, V. Sokolov, R. A. Levis, T. E. DeCoursey, Properties of single voltage-gated proton channels in human eosinophils estimated by noise analysis and by direct measurement. *J. General Physiol.* **121**, 615–628 (2003).

44. D. G. Levitt, Interpretation of biological ion channel flux data–reaction-rate versus continuum theory. *Annu. Rev. Biophys. Biophys. Chem.* **15**, 29–57 (1986).
45. B. Hille, *Ionic Channels of Excitable Membranes* (Sinauer Associates, Sunderland, MA, ed. 3, 2001).
46. D. E. Goldman, Potential, impedance, and rectification in membranes. *J. General Physiol.* **27**, 37–60 (1943).
47. T. E. DeCoursey, V. V. Cherny II, Voltage-activated proton currents in human THP-1 monocytes. *J. Membrane Biol.* **152**, 131–140 (1996).
48. S. M. E. Smith *et al.*, Voltage-gated proton channel in a dinoflagellate. *Proc. Natl. Acad. Sci. U.S.A.* **108**, 18162–18167 (2011).
49. T. E. DeCoursey, V. V. Cherny, Deuterium isotope effects on permeation and gating of proton channels in rat alveolar epithelium. *J. General Physiol.* **109**, 415–434 (1997).
50. S.-J. Marrink, H. J. C. Berendsen, Simulation of water transport through a lipid membrane. *J. Phys. Chem.* **98**, 4155–4168 (1994).
51. S. J. Marrink, H. J. C. Berendsen, Permeation process of small molecules across lipid membranes studied by molecular dynamics simulations. *J. Phys. Chem.* **100**, 16729–16738 (1996).
52. G. Parisio, M. Stocchero, A. Ferrarini, Passive membrane permeability: Beyond the standard solubility-diffusion model. *J. Chem. Theory Comput.* **9**, 5236–5246 (2013).
53. D. A. Doyle *et al.*, The structure of the potassium channel: Molecular basis of K+ conduction and selectivity. *Science* **280**, 69–77 (1998).
54. B. Roux, R. MacKinnon, The cavity and pore helices in the KcsA K+ channel: Electrostatic stabilization of monovalent cations *Science* **285**, 100–102 (1999).
55. S. Y. Noskov, B. Roux, Importance of hydration and dynamics on the selectivity of the KcsA and NaK channels. *J. General Physiol.* **129**, 135–143 (2007).
56. S. Y. Noskov, S. Berneche, B. Roux, Control of ion selectivity in potassium channels by electrostatic and dynamic properties of carbonyl ligands. *Nature* **431**, 830–834 (2004).
57. W. Im, B. Roux, Ion permeation and selectivity of OmpF porin: A theoretical study based on molecular dynamics, Brownian dynamics, and continuum electrodiffusion theory. *J. Mol. Biol.* **322**, 851–869 (2002).
58. R. Liang, H. Li, J. M. J. Swanson, G. A. Voth, Multiscale simulation reveals a multifaceted mechanism of proton permeation through the influenza A M2 proton channel. *Proc. Natl. Acad. Sci. U.S.A.* **111**, 9396–9401 (2014).
59. R. Liang *et al.*, Acid activation mechanism of the influenza A M2 proton channel. *Proc. Natl. Acad. Sci. U.S.A.* **113**, E6955 (2016).
60. H. T. Kratochvil *et al.*, Transient water wires mediate selective proton transport in designed channel proteins. *Nat. Chem.* **15**, 1012–1021 (2023).
61. P. Pohl *et al.*, Trapped pore waters in the open proton channel HV1. *Small* **19**, e2205968 (2023).
62. M. H. M. Olsson, C. R. Søndergaard, M. Rostkowski, J. H. Jensen, PROPKA3: Consistent treatment of internal and surface residues in empirical pKa predictions. *J. Chem. Theory Comput.* **7**, 525–537 (2011).
63. J. Huang *et al.*, CHARMM36m: An improved force field for folded and intrinsically disordered proteins. *Nat. Methods* **14**, 71–73 (2017).
64. J. Lee *et al.*, CHARMM-GUI input generator for NAMD, GROMACS, AMBER, OpenMM, and CHARMM/OpenMM simulations using the CHARMM36 additive force field. *J. Chem. Theory and Comput.* **12**, 405–413 (2016).
65. M. J. Abraham *et al.*, GROMACS: High performance molecular simulations through multi-level parallelism from laptops to supercomputers. *SoftwareX* **1–2**, 19–25 (2015).
66. C. Kutzner *et al.*, Best bang for your buck: GPU nodes for GROMACS biomolecular simulations. *J. Comput. Chem.* **36**, 1990–2008 (2015).
67. M. Parrinello, A. Rahman, Polymorphic transitions in single crystals: A new molecular dynamics method. *J. Appl. Phys.* **52**, 7182–7190 (1981).
68. G. Bussi, D. Donadio, M. Parrinello, Canonical sampling through velocity rescaling. *J. Chem. Phys.* **126**, 014101 (2007).
69. B. Hess, H. Bekker, H. J. C. Berendsen, J. G. E. M. Fraaije, LINCS: A linear constraint solver for molecular simulations. *J. Comput. Chem.* **18**, 1463–1472 (1997).
70. S. Plimpton, Fast parallel algorithms for short-range molecular dynamics. *J. Comput. Phys.* **117**, 1–19 (1995).
71. G. A. Tribello, M. Bonomi, D. Branduardi, C. Camilloni, G. Bussi, PLUMED 2: New feathers for an old bird. *Computer Phys. Commun.* **185**, 604–613 (2014).
72. T. W. Allen, O. S. Andersen, B. Roux, Energetics of ion conduction through the gramicidin channel. *Proc. Natl. Acad. Sci. U.S.A.* **01**, 117–122 (2004).
73. S. Kumar, J. M. Rosenberg, D. Bouzida, R. H. Swendsen, P. A. Kollman, The weighted histogram analysis method for free-energy calculations on biomolecules I. The method. *J. Comput. Chem.* **13**, 1011–1021 (1992).
74. H. J. C. Berendsen, J. R. Grigera, T. P. Straatsma, The missing term in effective pair potentials. *J. Phys. Chem.* **91**, 6269–6271 (1987).
75. Y. Wu, H. L. Tepper, G. A. Voth, Flexible simple point-charge water model with improved liquid-state properties. *J. Chem. Phys.* **124**, 024503 (2006).
76. B. Roux, O. S. Andersen, T. W. Allen, Comment on "Free energy simulations of single and double ion occupancy in gramicidin A" [J. Chem. Phys. 126, 105103 (2007)]. *J. Chem. Phys.* **128**, 105103 (2008).